

Specific Heat Capacity Determination by DSC

April 19, 10:00am - 11:00am EDT

Specific heat capacity (c_p) is an important, temperature-dependent material property and is often specified in material data sheets. It is a key property for improving technical processes such as injection molding, spray drying, or crystallization, as well as for the safety analysis of chemical processes and the design of chemical reactors.

Watch this session during the WAS Virtual Conference:



Dr. Jürgen Schawe

[Register Now](#)

This talk is sponsored by **METTLER TOLEDO**

Broadband Photoconductive Sampling in Gallium Phosphide

Najd Altwaijry, Muhammad Qasim, Mikhail Mamaikin, Johannes Schötz, Keyhan Golyari, Michael Heynck, Enrico Ridente, Vladislav S. Yakovlev, Nicholas Karpowicz,* and Matthias F. Kling*

Direct measurements of the electric field of light enable new observations of light–matter interactions. In the near-infrared and visible spectral ranges, this typically relies on techniques that exploit nonlinearities in gases or solids, which limits their sensitivity. Here, a method for the detection of broadband near-infrared fields spanning more than one octave from 110 to 220 THz based on linear absorption in a semiconductor is demonstrated. This technique, which avoids complex vacuum setups and works under ambient conditions, employs linear photoconductive sampling (LPS) in gallium phosphide. Simulations reveal that the response function of LPS is concerned with the intensity envelope of the gate field, in contrast to electro-optic sampling, relaxing the stringent temporal requirements on the gate pulse.

1. Introduction

Access to the information encoded in the evolution of the electric field of light as it interacts with atoms, molecules and solids is a powerful tool in modern ultrafast science. The detailed,

time-resolved picture it provides^[1] opens the door for coherent control of electron dynamics in such systems. Most measurement techniques, which provide access to terahertz and petahertz scale electric fields, such as attosecond streaking,^[2,3] use an ultrashort gate pulse to sample the electric field under study at a given instant in time, and read out the full waveform with a variable time delay. In the optical domain, attosecond streaking has been routinely used to explore and control electron^[4–6] and spin^[7] dynamics in solids. It has also been applied to measure photoemission delays in molecular,^[8–10] nano,^[11] and liquid systems.^[12,13] Although

a powerful tool for characterizing electric fields on the shortest timescale possible, attosecond streaking requires complex ultra-high vacuum infrastructure and intense laser sources, which limits the widespread accessibility of the technique. For these reasons, compact and flexible alternatives are highly coveted.

An example of techniques that work under ambient conditions is all-optical electro-optic sampling (EOS), a technique originating from the terahertz community^[14–16] that has been recently extended to the near-infrared (NIR)^[17] and visible ranges.^[18] Here, the sampled field changes the polarization state of the gate pulse in a nonlinear crystal which can be measured using an ellipsometer to reconstruct the waveform. The co-propagation of the fields in a nonlinear crystal leads to phase-matching limitations, in addition to difficulties in expanding EOS farther into the visible range, as this would require ultraviolet gate pulses close to the absorption edges of most common nonlinear crystals.


An alternative is presented by techniques that rely on the measurement of strong-field-induced charge carriers, such as nonlinear photoconductive sampling (NPS)^[19] and tunneling ionization with a perturbation for the time-domain observation of an electric field (TIPTOE).^[20–24] NPS relies on free carrier generation in a gas^[25,26] or solid^[19] between two electrodes with an ultrashort gate pulse, where the gate pulse is polarized perpendicular to the electrode axis. The carriers are then driven by a waveform-stable field, polarized along the electrode axis, causing a macroscopic current. Measuring the induced current as a function of delay between the gate pulse and driving field permits the retrieval of the electric field of the latter. Similarly, TIPTOE uses a strong laser pulse to induce free carrier generation in a medium between two electrodes, perturbed by a weak electric field one wishes to sample.

N. Altwaijry, M. Qasim, M. Mamaikin, J. Schötz, K. Golyari, M. Heynck, E. Ridente, V. S. Yakovlev, N. Karpowicz, M. F. Kling
Division of Attosecond Physics
Max Planck Institute of Quantum Optics
85748, Garching, Germany
E-mail: nicholas.karpowicz@mpq.mpg.de

N. Altwaijry, M. Qasim, M. Mamaikin, J. Schötz, K. Golyari, M. Heynck, E. Ridente, V. S. Yakovlev, N. Karpowicz, M. F. Kling
Department of Physics
Ludwig-Maximilians-Universität
85748, Garching, Germany

M. F. Kling
PULSE Institute
SLAC National Accelerator Laboratory
Menlo Park, CA 94025, USA

M. F. Kling
Applied Physics Department
Stanford University
Stanford, CA 94305, USA
E-mail: kling@stanford.edu

 The ORCID identification number(s) for the author(s) of this article can be found under <https://doi.org/10.1002/adom.202202994>.

© 2023 The Authors. Advanced Optical Materials published by Wiley-VCH GmbH. This is an open access article under the terms of the Creative Commons Attribution License, which permits use, distribution and reproduction in any medium, provided the original work is properly cited.

DOI: 10.1002/adom.202202994

These photoconductive techniques require waveform-controlled strong-field gate pulses and nonlinearities for carrier generation. The terahertz community has long used field measurements based on the Auston switch^[27] without this requirement. Linear photoconductive sampling (LPS) does not require an intense gate pulse and its response to fields oscillating much more slowly than the gate pulse carrier frequency is independent of carrier-envelope phase. The gating mechanism is not temporally confined by nonlinearity however, placing stricter requirements on the pulse duration. Nonetheless, LPS has successfully been applied from the THz through the mid-infrared,^[28,29] with advancements extending the cutoff from 60 THz^[30] to 100 THz.^[31]

Here, we further expand the broadband detection range of LPS. We demonstrate that a visible–near-ultraviolet (VIS–UV) pulse provides a short enough temporal gate to resolve frequencies over 200 THz in a common semiconductor. We relied on gallium phosphide (GaP), a relatively cheap and stable low band-gap material. Moreover, the simplicity of our setup, avoiding any vacuum infrastructure, makes ultrafast current detection widely accessible and feasible for applications in optoelectronic signal control and processing.

2. Experimental Section

The signal in LPS is generated as follows: first, an ultrashort gate pulse linearly injects charge carriers in a medium through single-photon absorption (see Section S1, Supporting Information). In the case of solids, this pulse excited an electron from the valence band to the conduction band of the material, as depicted in the inset of Figure 1a.^[32] Second, both the electron and hole that emerged in the conduction and valence band respectively can be displaced by a driving pulse, separating

the charges spatially and forming a dipole. The acceleration of the charges by the driving field was governed by Bloch's acceleration theorem,^[33] which stated that the rate of change in the electron's crystal momentum was proportional to the applied external field: $\hbar k' = eE_D$. Here k is the projection of the electron's crystal momentum and E_D is the external driving field. Finally, by contacting the sample with electrodes and scanning the delay τ between the two pulses, an electric current was detected through an external circuit. For simplicity, direct currents reaching the electrodes were neglected due to the short mean free path of carriers in the solid, which was typically an order of magnitude smaller than the separation of the electrodes. To a first order approximation, the detected current was directly proportional to the vector potential of the driving pulse $j(\tau) \propto \rho A_D(\tau)$, where ρ is the generated carrier density in the sample and A_D is the vector potential, the derivative of which is the electric field of the driving pulse following $A_D(t) = -E_D(t)$.

The laser system used in the experiment is described in detail in ref. [34]. Briefly, 15 fs duration pulses at 1.8 μm central wavelength with 1 mJ pulse energy were obtained from a home-built optical parametric chirped pulse amplifier (OPCPA) and spectrally broadened in an air-filled hollow-core fiber, generating an ultrabroadband spectrum spanning three octaves from 300–3000 nm. As illustrated in Figure 1b, this spectrum was split into three channels, each channel spanning approximately one octave in bandwidth. The channels were individually compressed using custom-made chirped mirrors.^[18] Here, the VIS–UV pulse spanning ≈ 300 –600 nm was used as the carrier injection gate pulse. The sampled field used to drive the excited carriers was the NIR pulse spanning 1400–2700 nm. The two pulses were delayed with respect to each other in a Mach–Zehnder type interferometer, where both fields were polarized in the same vertical direction. To separate the signal from background noise a lock-in amplifier was used during the measure-

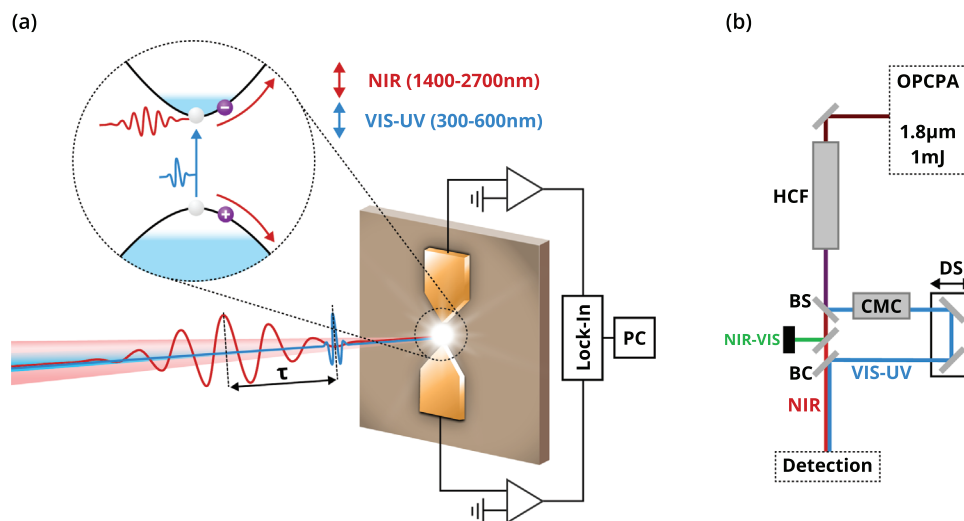


Figure 1. a) Schematic of LPS detection. The NIR field (in red) is delayed by τ with respect to the VIS–UV field (in blue). Both fields are polarized along the orientation of the electrodes. The electrode separation is 400 μm and the beam spot size is 50 μm . The inset illustrates LPS in reciprocal space: the VIS–UV field excites an electron from the valence to the conduction band of GaP, the NIR field drives the electron–hole pair in the conduction and valence bands, respectively. b) Sketch of the experimental setup. The output from the OPCPA is broadened in a hollow-core fiber (HCF) and split into three channels using beamsplitters (BS). A chirped mirror compressor (CMC) is used to compensate dispersion and achieve VIS–UV pulses with durations down to 2.7 fs.^[18] After recombination using a beam combiner (BC), the pulses are focused into GaP. The electric field of the NIR pulse is sampled by varying the relative time between the two pulses using a delay stage (DS).

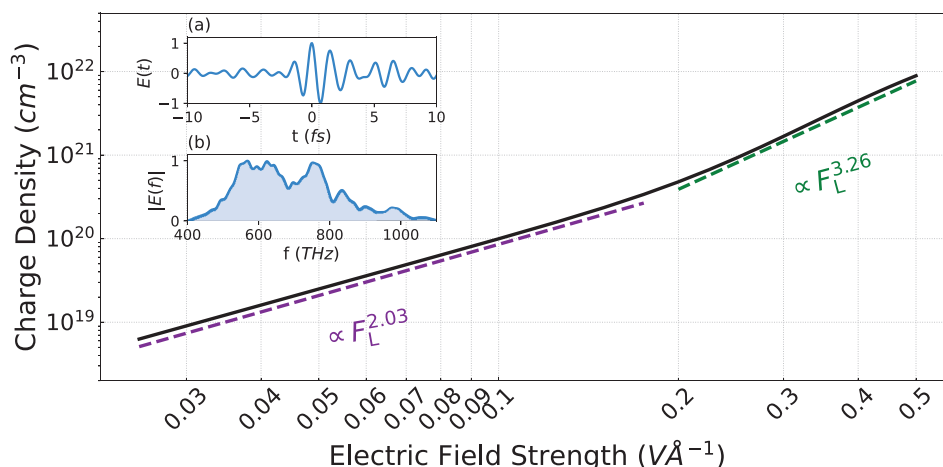


Figure 2. Calculated relationship between the VIS–UV field strength (inset a) and charge density generated in GaP. In the regime depicted by the purple dashed line, the VIS–UV pulse injects the carriers linearly. Insets: a) The waveform of the VIS–UV pulse and b) the absolute value of its Fourier transform.

ment. To further reduce the noise level, the carrier envelope phase of the fields was alternately flipped by π using an acousto-optic dispersive programmable filter (Fastlite DAZZLER) and the modulation was recorded at half the laser repetition rate.

The field (Figure 2a) and spectrum (Figure 2b) of the VIS–UV injection pulse were independently characterized by NPS.^[18] In the experiment, a GaP crystal (L-cut, indirect band-gap 2.24 eV, direct band-gap 2.78 eV^[35]) was utilized to excite carriers primarily via single-photon absorption. In order to derive the criteria for linear injection, the VIS–UV induced charge density was calculated in GaP as a function of peak field strengths of the laser using the method described in ref. [36]. The dependence of the computed charge density on the peak electric field was compared with a polynomial scaling characteristic of both single and multi-photon absorption.^[37] In the perturbative limit, the cycle-averaged transition rate, and subsequently the excited charge density, was approximately proportional to F^{2N} , where F is the peak field strength of the excitation pulse and N indicates the number of photons participating in a transition. In Figure 2, it is shown how the carrier charge density scales with the peak field strength of the VIS–UV pulse. The dashed lines indicated the different scaling regimes. At moderate field strengths below 0.1 VÅ^{-1} , the excited carrier density scales according to F^2 as indicated by the purple dashed line. In this regime, the excitation was mainly dominated by single-photon absorption, hence the charge density increased linearly with the peak intensity of the laser field. For $F > 0.1 \text{ VÅ}^{-1}$, the charge density grows nonlinearly as shown by the green dashed line, where the scaling law was $\propto F^{3.26}$, which resulted in $N \approx 2$, highlighting the fact that the two-photon absorption was mainly responsible for the generation of charge carriers. The regime of linear absorption was thus limited to field strengths below 0.1 VÅ^{-1} . By carefully selecting the laser parameters, a VIS–UV field strength of $F = 0.08 \text{ VÅ}^{-1}$ was maintained throughout the experiment. Moreover, the highest frequency in the measured field corresponded to 0.89 eV, well below the band-gap of GaP. To rule out nonlinear injection, the field strength of the NIR field was reduced experimentally via a reflective filter.

3. Results

The waveform of the NIR field as measured by means of LPS is illustrated in Figure 3a in blue. Figure 3b depicts the absolute value of the Fourier transformed waveforms from Figure 3a. Under identical experimental conditions, we performed EOS of the NIR field in a 5 μm beta-barium borate (BBO) crystal, where the VIS–UV pulse acted as a gate pulse. As can be seen in Figure 3a, the two waveforms exhibit considerable similarity, signified by a $r = 0.79$ correlation coefficient. Similarly, the spectra obtained by both sampling techniques display significant overlap as well, despite the difference in the physical origins of the signal obtained through each detection scheme.

Figure 4 illustrates the spectral responses of both EOS and LPS, respectively. To calculate the response function of EOS, we numerically propagated a VIS–UV pulse centered around 750 THz with a bandwidth of 300 THz along with a broadband NIR field centered at 210 THz with a bandwidth of 180 THz under varying time delays using the equation^[38]

$$(\partial_z - ik(\omega))\mathbf{E}(\mathbf{r}, \omega) = \frac{i}{2k(\omega)} \nabla_{\perp}^2 \mathbf{E}(\mathbf{r}, \omega) + \frac{i\omega}{2\epsilon_0 n(\omega)c} \mathbf{P}_{\text{NL}}(\mathbf{r}, \omega) \quad (1)$$

where \mathbf{E} is the electric field of light, \mathbf{P}_{NL} is the nonlinear polarization, $k(\omega)$ is the wavevector, $n(\omega)$ is the refractive index under the slowly varying amplitude approximation. The propagation was done in a Type I BBO crystal with a phase matching angle of $\theta = 24^\circ$. The nonlinear polarization is calculated using the second and third order nonlinear tensors of BBO. The response is then calculated by computing the ratio between the EOS signal (change in the polarization state of the VIS–UV field) to the input NIR field. Furthermore, the thickness of the BBO crystal was varied from 10 to 100 μm to obtain Figure 4c.

Likewise, to calculate the response function of LPS (Figure 4b), we modeled the interaction of a VIS–UV few-cycle intense pulse and a NIR infrared drive pulse in GaP using the method described in ref. [36]. To this end, we solved the 3D time-dependent Schrödinger equation in the stationary basis of Kohn–Sham orbitals. In this formalism, the electronic

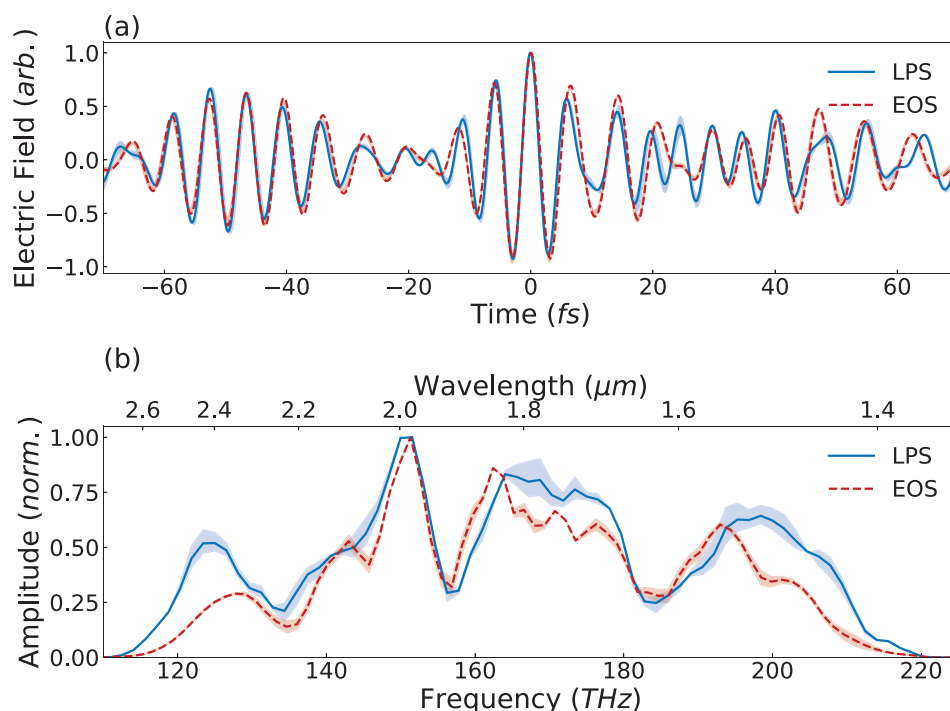


Figure 3. a) The recorded waveforms of the NIR field detected via LPS (blue, the shaded area represents the standard deviation of three measured traces) and EOS (red dashed). b) Corresponding spectra of the waveforms in (a). The standard deviation is represented by the shaded area around the curves.

structure of GaP is described by band energies and transition matrix elements, obtained from density functional theory utilizing the Tran–Blaha exchange–correlation potential,^[39] and calculated using the ELK code.^[40] We used two time-delayed laser fields: the VIS–UV 2.7 fs, centered ≈ 650 THz with a maximum field strength of 0.05 V \AA^{-1} for injecting carriers in GaP and a 6 fs weak NIR probing field of 0.01 V \AA^{-1} , centered at 165 THz to evaluate the occupation probabilities under several different delays. From that, the drift current in the medium is calculated as a function of delays between the VIS–UV pulse and the NIR pulse. The vector potential of the probing NIR field is then evaluated by performing a fast Fourier transform of the drift current. Due to its proportionality to the drift current, information about the response of the system is contained and retrieved by dividing the fast Fourier transform of the drift current signal by the original NIR probing field. Note that the parameters chosen for the analysis of the response functions of both LPS and EOS are optimized for the analyzed spectral range.

4. Discussion and Conclusion

The complex spectral response of EOS, in the limit of a thin crystal, can be calculated as

$$S_{\text{EOS}}(\Omega) = \int_{-\infty}^{\infty} d\omega R(\omega) |E(\omega)| |E(\omega - \Omega)| e^{i[\phi(\omega) - \phi(\omega - \Omega)]} \quad (2)$$

where ω and Ω represent spectral components in the VIS–UV and NIR fields, respectively.^[17] Note that the relative phase of

two spectral components, the one serving as the input to the sum frequency ($\omega - \Omega$), and the one serving as the local oscillator (ω), can affect the measured signal. A shift in carrier-envelope phase does not influence the EOS response, but higher order terms of the spectral phase, such as chirp, can reshape the response function.

To demonstrate this effect we calculated the EOS response for several VIS–UV pulses with different second order phases as seen in Figure 4a. The relationship between EOS sensitivity and the VIS–UV field shape highlights the importance of a compressed gate field for EOS. Particularly, in the case of $\pm 5 \text{ fs}^2$, the EOS response is reduced by 38 dB. In contrast, the response function of LPS, illustrated in Figure 4b, is relatively flat across most of the frequency range examined regardless of the gating field compression, signifying LPS's dependency on the VIS–UV envelope rather than field. This observation is corroborated by the symmetry between positive and negative chirp values. The reason behind this is because the original phase information of the gate field is lost after it is absorbed and the temporal profile of the response is a result of the carrier density only.

An additional advantage of photoconductive sampling is the ability to sample a large bandwidth without phase-matching limitations. This is in contrast to EOS, which depends on non-linear frequency mixing.^[41] From Figure 4c, it can be discerned that the bandwidth of the response function of EOS is inversely proportional to the thickness of the crystal, thereby making it extremely difficult to measure broadband pulses and especially weak signals, where a thicker crystal would be advantageous. Moreover, the choice of bandpass filter used in EOS influences

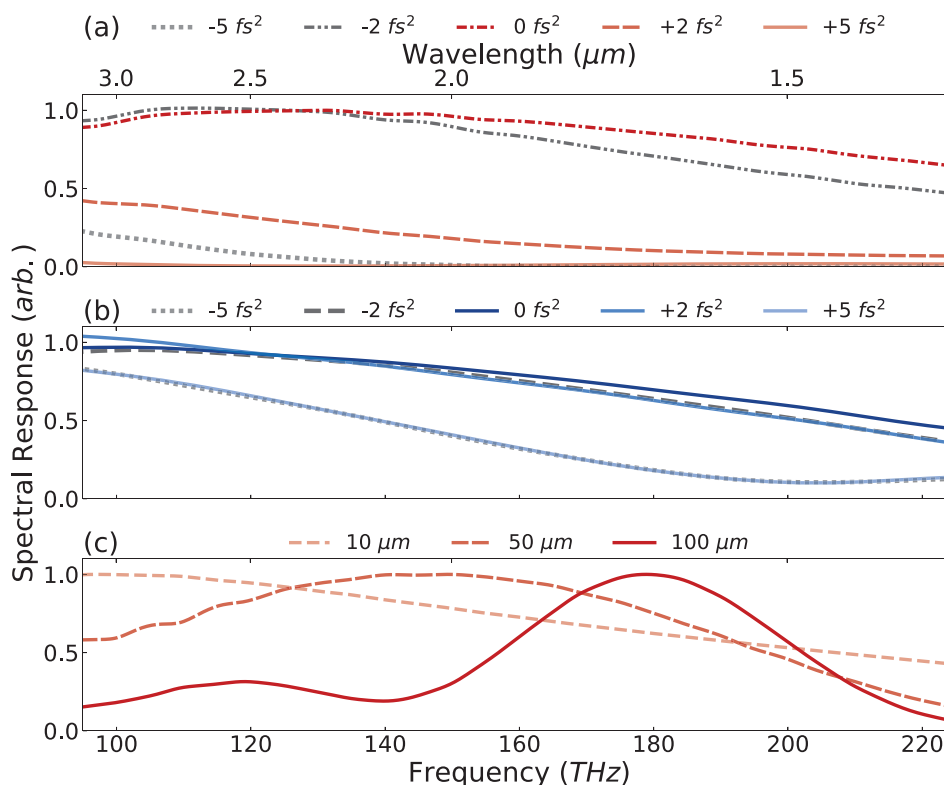


Figure 4. a) EOS (in red) and b) LPS (in blue) spectral response functions calculated with different GDD values applied to the VIS–UV pulse. c) EOS response calculated for a compressed VIS–UV pulse and different crystal thicknesses.

the response function, making the choice of spectral filter an additional constraint for EOS (see Section S1, Supporting Information).

Furthermore, when compared to NPS, LPS offers a cleaner detection mechanism by virtue of injecting a single electron with a well-defined wavepacket in a single well-defined band, as opposed to generating multiple electron wavepackets that occupy multiple bands, smearing out information and preventing reliable retrieval of the waveform as is the case in NPS.^[32] Finally, our implementation of LPS supports the possibility of measuring the electric field in two spatial dimensions simultaneously, for example, for measuring elliptically or circularly polarized light. This offers an advantage over other techniques such as NPS, which conventionally relies on the use of two orthogonally polarized pulses. Similarly, in the case of EOS, it would require consecutive measurements with different crystal orientations.^[42]

In conclusion, we have demonstrated an alternative method for sampling near-infrared fields under ambient conditions without the need for a complex vacuum setup. We have used a widely accessible solid-state material. Our method overcomes some of the technical and physical limitations of streaking, EOS and NPS. As a simple all-solid-state metrology technique, our method can be easily incorporated into any infrastructure, opening the door for sensitive field measurements and for well-defined probing of electron dynamics in solids.

Supporting Information

Supporting Information is available from the Wiley Online Library or from the author.

Acknowledgements

The authors are grateful to Ferenc Krausz for fruitful discussions and for providing suitable laboratory space at MPQ. This work is supported by the European Union under grant EU-H2020 654148 (Laserlab Europe) and the FETOpen project PetaCOM. The authors acknowledge support by the Air Force Office of Scientific Research under grant FA9550-16-1-0073. M.F.K.'s work at SLAC is supported by the U.S. Department of Energy, Office of Science, Basic Energy Sciences, Scientific User Facilities Division, under Contract No. DE-AC02-76SF00515. N.A. is part of the Max Planck School of Photonics supported by BMBF, Max Planck Society, and Fraunhofer Society. N.A., M.Q., K.G., and E.R. acknowledge support by the Max Planck Society via the IMPRS for Advanced Photon Science.

Open access funding enabled and organized by Projekt DEAL.

Conflict of Interest

The authors declare no conflict of interest.

Data Availability Statement

The data that support the findings of this study are available from the corresponding author upon reasonable request.

Keywords

field sampling metrology, laser science, strong-field physics, ultrafast optics

Received: December 13, 2022

Revised: January 24, 2023

Published online:

- [1] A. Sommer, E. M. Bothschafter, S. A. Sato, C. Jakubeit, T. Latka, O. Razskazovskaya, H. Fattahi, M. Jobst, W. Schweinberger, V. Shirvanyan, V. S. Yakovlev, R. Kienberger, K. Yabana, N. Karpowicz, M. Schultze, F. Krausz, *Nature* **2016**, 534, 86.
- [2] F. Krausz, M. Ivanov, *Rev. Mod. Phys.* **2009**, 81, 163.
- [3] R. Kienberger, E. Goulielmakis, M. Uiberacker, A. Baltuska, V. Yakovlev, F. Bammer, A. Scrinzi, T. Westerwalbesloh, U. Kleineberg, U. Heinzmann, M. Drescher, F. Krausz, *Nature* **2004**, 427, 817.
- [4] E. Goulielmakis, V. S. Yakovlev, A. L. Cavalieri, M. Uiberacker, V. Pervak, A. Apolonski, R. Kienberger, U. Kleineberg, F. Krausz, *Science* **2007**, 317, 769.
- [5] A. L. Cavalieri, N. Müller, T. Uphues, V. S. Yakovlev, A. Baltuska, B. Horvath, B. Schmidt, L. Blümel, R. Holzwarth, S. Hendel, M. Drescher, U. Kleineberg, P. M. Echenique, R. Kienberger, F. Krausz, U. Heinzmann, *Nature* **2007**, 449, 1029.
- [6] M. Schultze, E. M. Bothschafter, A. Sommer, S. Holzner, W. Schweinberger, M. Fiess, M. Hofstetter, R. Kienberger, V. Apalkov, V. S. Yakovlev, M. I. Stockman, F. Krausz, *Nature* **2013**, 493, 75.
- [7] F. Siegrist, J. A. Gessner, M. Ossiander, C. Denker, Y.-P. Chang, M. C. Schröder, A. Guggenmos, Y. Cui, J. Walowski, U. Martens, J. K. Dewhurst, U. Kleineberg, M. Münzenberg, S. Sharma, M. Schultze, *Nature* **2019**, 571, 240.
- [8] M. Huppert, I. Jordan, D. Baykusheva, A. von Conta, H. J. Wörner, *Phys. Rev. Lett.* **2016**, 117, 093001.
- [9] J. Vos, L. Cattaneo, S. Patchkovskii, T. Zimmermann, C. Cirelli, M. Lucchini, A. Kheifets, A. S. Landsman, U. Keller, *Science* **2018**, 360, 1326.
- [10] S. Biswas, B. Förg, L. Ortmann, J. Schötz, W. Schweinberger, T. Zimmermann, L. Pi, D. Baykusheva, H. A. Masood, I. Lontos, A. M. Kamal, N. G. Kling, A. F. Alharbi, M. Alharbi, A. M. Azzeer, G. Hartmann, H. J. Wörner, A. S. Landsman, M. F. Kling, *Nat. Phys.* **2020**, 16, 778.
- [11] L. Seiffert, Q. Liu, S. Zhrebtsov, A. Trabattani, R. Rupp, M. C. Castrovilli, M. Galli, F. Süßmann, K. Wintersperger, J. Stierle, G. Sansone, L. Poletto, F. Frassetto, I. Halfpap, V. Mondes, C. Graf, E. Rühl, F. Krausz, M. Nisoli, T. Fennel, F. Calegari, M. F. Kling, *Nat. Phys.* **2017**, 13, 766.
- [12] I. Jordan, M. Huppert, D. Rattenbacher, M. Peper, D. Jelovina, C. Perry, A. von Conta, A. Schild, H. J. Wörner, *Science* **2020**, 369, 974.
- [13] X. Gong, I. Jordan, M. Huppert, S. Heck, D. Baykusheva, D. Jelovina, A. Schild, H. J. Wörner, *CHIMIA* **2022**, 76, 520.
- [14] J. A. Valdmanis, G. Mourou, C. W. Gabel, *Appl. Phys. Lett.* **1982**, 41, 211.
- [15] C. Kübler, R. Huber, S. Tübel, A. Leitenstorfer, *Appl. Phys. Lett.* **2004**, 85, 3360.
- [16] A. Leitenstorfer, S. Hunsche, J. Shah, M. C. Nuss, W. H. Knox, *Appl. Phys. Lett.* **1999**, 74, 1516.
- [17] S. Keiber, S. Sederberg, A. Schwarz, M. Trubetskov, V. Pervak, F. Krausz, N. Karpowicz, *Nat. Photonics* **2016**, 10, 159.
- [18] E. Ridente, M. Mamaikin, N. Altwaijry, D. Zimin, M. F. Kling, V. Pervak, M. Weidman, F. Krausz, N. Karpowicz, *Nat. Commun.* **2022**, 13, 1111.
- [19] S. Sederberg, D. Zimin, S. Keiber, F. Siegrist, M. S. Wismer, V. S. Yakovlev, I. Floss, C. Lemell, J. Burgdörfer, M. Schultze, F. Krausz, N. Karpowicz, *Nat. Commun.* **2020**, 11, 430.
- [20] S. B. Park, K. Kim, W. Cho, S. I. Hwang, I. Ivanov, C. H. Nam, K. T. Kim, *Optica* **2018**, 5, 402.
- [21] Y. Liu, S. Gholam-Mirzaei, J. E. Beetar, J. Nesper, A. Yousif, M. Nrisimhamurthy, M. Chini, *Photonics Res.* **2021**, 9, 929.
- [22] Y. Liu, J. E. Beetar, J. Nesper, S. Gholam-Mirzaei, M. Chini, *Nat. Photonics* **2022**, 16, 109.
- [23] M. R. Bionta, F. Ritzkowski, M. Turchetti, Y. Yang, D. Cattozzo Mor, W. P. Putnam, F. X. Kärtner, K. K. Berggren, P. D. Keathley, *Nat. Photonics* **2021**, 15, 456.
- [24] J. Blöchl, J. Schötz, A. Maliakkal, N. Šreibere, Z. Wang, P. Rosenberger, P. Hommelhoff, A. Staudte, P. B. Corkum, B. Bergues, M. F. Kling, *Optica* **2022**, 9, 755.
- [25] A. Korobenko, K. Johnston, M. Kubulek, L. Arissian, Z. Dube, T. Wang, M. Kübel, A. Y. Naumov, D. M. Villeneuve, M. F. Kling, P. B. Corkum, A. Staudte, B. Bergues, *Optica* **2020**, 7, 1372.
- [26] D. Zimin, M. Weidman, J. Schötz, M. F. Kling, V. S. Yakovlev, F. Krausz, N. Karpowicz, *Optica* **2021**, 8, 586.
- [27] D. H. Auston, *Appl. Phys. Lett.* **1975**, 26, 101.
- [28] M. Tani, S. Matsuura, K. Sakai, S. ichi Nakashima, *Appl. Opt.* **1997**, 36, 7853.
- [29] Y. C. Shen, P. C. Upadhy, H. E. Beere, E. H. Linfield, A. G. Davies, I. S. Gregory, C. Baker, W. R. Tribe, M. J. Evans, *Appl. Phys. Lett.* **2004**, 85, 164.
- [30] S. Kono, M. Tani, K. Sakai, *IEEE Proc. Optoelectr.* **2002**, 149, 105.
- [31] M. Ashida, *Jap. J. Appl. Phys.* **2008**, 47, 8221.
- [32] M. Ossiander, K. Golyari, K. Scharl, L. Lehnert, F. Siegrist, J. P. Bürger, D. Zimin, J. A. Gessner, M. Weidman, I. Floss, V. Smejkal, S. Donsa, C. Lemell, F. Libisch, N. Karpowicz, J. Burgdörfer, F. Krausz, M. Schultze, *Nat. Commun.* **2022**, 13, 1620.
- [33] F. Bloch, *Z. Phys.* **1929**, 52, 555.
- [34] E. Ridente, M. Weidman, M. Mamaikin, C. Jakubeit, F. Krausz, N. Karpowicz, *Optica* **2020**, 7, 1093.
- [35] R. Zallen, W. Paul, *Phys. Rev.* **1964**, 134, A1628.
- [36] M. Qasim, D. A. Zimin, V. S. Yakovlev, *Phys. Rev. Lett.* **2021**, 127, 087401.
- [37] L. V. Keldysh, *J. Exp. Theor. Phys.* **1965**, 20, 1307.
- [38] T. Brabec, F. Krausz, *Phys. Rev. Lett.* **1997**, 78, 3282.
- [39] F. Tran, P. Blaha, *Phys. Rev. Lett.* **2009**, 102, 226401.
- [40] The elk code, <http://elk.sourceforge.io> (accessed: June 2022).
- [41] G. Gallot, D. Grischkowsky, *J. Opt. Soc. Am. B* **1999**, 16, 1204.
- [42] L. Zhang, H. Zhong, C. Deng, C. Zhang, Y. Zhao, *Appl. Phys. Lett.* **2009**, 94, 211106.